Earth and Planetary Science Letters 396 (2014) 78–87

Contents lists available at ScienceDirect

Earth and Planetary Science Letters

www.elsevier.com/locate/epsl

Sound velocity of Fe–S liquids at high pressure: Implications for the Moon's molten outer core

Zhicheng Jing [a,b,*], Yanbin Wang [a], Yoshio Kono [c], Tony Yu [a], Tatsuya Sakamaki [a,1], Changyong Park [c], Mark L. Rivers [a], Stephen R. Sutton [a], Guoyin Shen [c]

[a] Center for Advanced Radiation Sources, The University of Chicago, Chicago, IL 60637, USA
[b] Department of Earth, Environmental, and Planetary Sciences, Case Western Reserve University, Cleveland, OH 44106, USA
[c] HPCAT, Carnegie Institution of Washington, Argonne, IL 60439, USA

ARTICLE INFO

Article history:
Received 23 October 2013
Received in revised form 31 March 2014
Accepted 6 April 2014
Available online xxxx
Editor: L. Stixrude

Keywords:
Fe–S liquid
velocity
density
equation of state
high pressure
lunar core

ABSTRACT

Sound velocities of Fe and Fe–S liquids were determined by combining the ultrasonic measurements and synchrotron X-ray techniques under high pressure–temperature conditions from 1 to 8 GPa and 1573 K to 1973 K. Four different liquid compositions were studied including Fe, Fe–10 wt% S, Fe–20 wt% S, and Fe–27 wt% S. Our data show that the velocity of Fe-rich liquids increases upon compression and decreases with increasing sulfur content, whereas temperature has negligible effect on the velocity of Fe–S liquids. The sound velocity data were combined with ambient-pressure densities to fit the Murnaghan equation of state (EOS). Compared to the lunar seismic model, our velocity data constrain the sulfur content at 4 ± 3 wt%, indicating a significantly denser (6.5 ± 0.5 g/cm^3) and hotter (1870^{+100}_{-70} K) outer core than previously estimated. A new lunar structure model incorporating available geophysical observations points to a smaller core radius. Our model suggests a top–down solidification scenario for the evolution of the lunar core. Such "iron snow" process may have been an important mechanism for the growth of the inner core.

© 2014 Elsevier B.V. All rights reserved.

1. Introduction

Geophysical observations based on lunar seismology (Lognonné and Johnson, 2007; Weber et al., 2011) and laser ranging (Williams et al., 2001) strongly suggest that the Moon's iron core is partially molten. Similar to Earth and other terrestrial planets, light elements, such as sulfur, silicon, carbon, and oxygen, etc., are likely present in the lunar core (Li and Fei, 2003), significantly affecting the density and freezing temperature of the core. Determining the light element concentration in the outer core is of vital importance to the understanding of the structure, dynamics, and chemical evolution of the Moon, as well as the enigmatic history of the lunar dynamo (Shea et al., 2012). However, the exact composition of the outer core is poorly constrained by comparing laboratory density data of iron-rich liquids with geophysical observations due to the large uncertainties in density measurements and the non-unique core density inversion from observations.

Sulfur is the preferred major light element in the lunar outer core over other elements due to its high abundance in the parent bodies of iron meteorites (Chabot, 2004), its high solubility in liquid Fe (Buono and Walker, 2011) compared to other light elements at the lunar core pressure (~5 GPa, Garcia et al., 2011), and its strong effects on reducing the density, velocity, and freezing temperature of the core (e.g., Buono and Walker, 2011; Sanloup et al., 2000). In contrast, silicon and oxygen likely increase the velocity of liquid Fe (Huang et al., 2011; Sanloup et al., 2004).

Comparing sound velocity data to lunar seismic models provides a direct approach to infer the composition of the lunar outer core. In the past, velocities of Fe-rich liquids at high pressures were indirectly estimated from density measurements under static compression (Sanloup et al., 2000, 2004). Such estimation suffers from a large trade-off between density and compressibility (which is related to the pressure dependence of density) due to the limited pressure range (0–6 GPa) of the measurements and the scarcity and inherent large uncertainties of the density data. High-pressure velocity measurements on liquids are technically challenging. Previous measurements on the sound velocity of Fe-rich liquids were

* Corresponding author at: Department of Earth, Environmental, and Planetary Sciences, Case Western Reserve University, Cleveland, OH 44106, USA. Tel.: +1 216 368 2316.
E-mail address: zhicheng.jing@case.edu (Z. Jing).
[1] Present address: Department of Earth Science, Tohoku University, Sendai 980-8578, Miyagi, Japan.

http://dx.doi.org/10.1016/j.epsl.2014.04.015
0012-821X/© 2014 Elsevier B.V. All rights reserved.

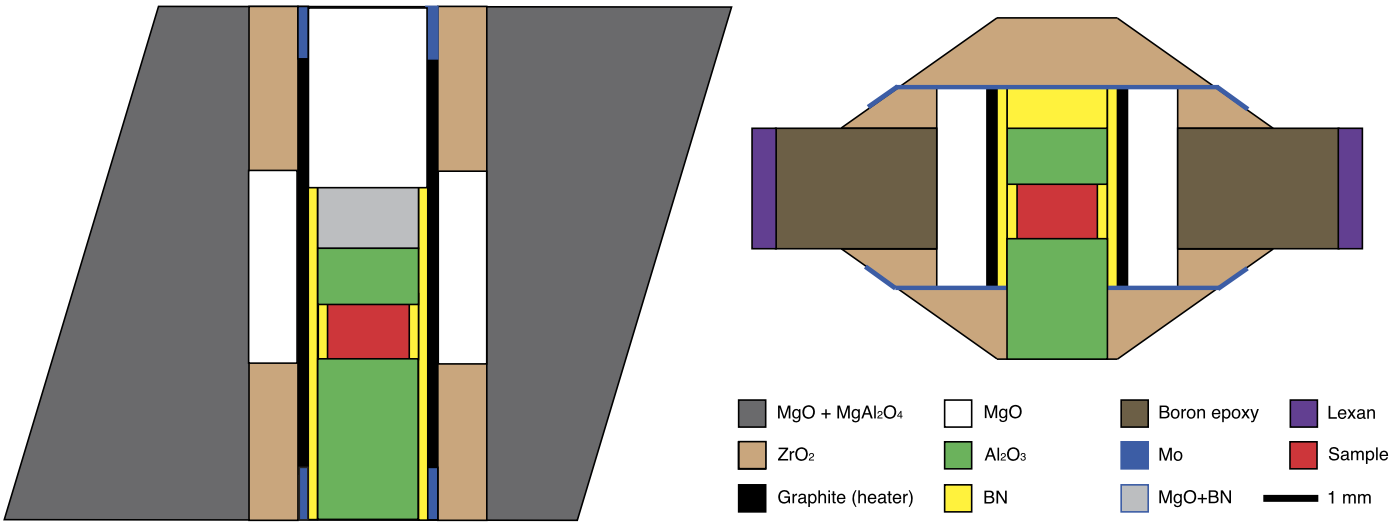

Fig. 1. Schematic drawings of cell assemblies used in the experiments. The left figure shows the assembly used in multi-anvil experiments, and the right figure shows the one used in PE experiments.

mostly performed at ambient pressure (Hixson et al., 1990; Nasch et al., 1997). High pressure measurements from a very recent study (Nishida et al., 2013) were limited to only one liquid composition (Fe–30 wt% S). Shock-wave data on velocities of Fe-rich liquids (Anderson and Ahrens, 1994; Huang et al., 2011) were obtained at much higher pressures (70–400 GPa) and temperatures, far exceeding the conditions in the lunar core.

In this study, we conducted measurements on the sound velocity of Fe and Fe–S liquids under deep Moon pressure–temperature conditions. Results of these measurements were directly compared to the seismic velocity of the lunar outer core to provide constraints on the sulfur content, density, temperature, and solidification regime of the outer core.

2. Experimental methods

We performed *in-situ* measurements on travel times of ultrasonic sound waves through liquid samples under high pressure and temperature conditions up to 8 GPa and 1973 K. Synchrotron X-ray diffraction and radiographic imaging techniques allowed simultaneous determination of pressure and sample lengths, respectively, yielding sound velocities from the travel time measurements.

High pressure–temperature conditions were generated using both the Kawai-type multi-anvil device (MA) (Wang et al., 2009) at the GSECARS beamline 13-ID-D of APS and the Paris–Edinburgh device (PE) (Kono et al., 2012) at the HPCAT beamline 16-BM-B. In MA experiments, second-stage tungsten carbide (WC) anvils with 8-mm truncation edge length (TEL) were used. An injection molded octahedral $MgO–MgAl_2O_4$ pressure medium with 14-mm edge length (Leinenweber et al., 2012) was used in each experiment. In PE experiments, a pair of cup-shape WC anvils with 3 mm diameter flat bottoms was used. Boron-epoxy rings and ZrO_2 caps were used as pressure medium. Fig. 1 shows schematically the cell assemblies used in both devices. In each experiment, an Al_2O_3 (fully densified) buffer rod (BR), was placed between the WC anvil and the sample to (1) enhance the propagation of elastic waves, (2) define the position of the sample in X-ray images, and (3) provide sufficient impedance contrast to reflect ultrasonic waves at the BR-sample interface. The sample was inserted into a boron nitride (BN) sleeve capsule and sandwiched by an Al_2O_3 backing plate (BP), which was used to maintain the flatness of the sample after melting and reflect waves back at the sample-BP interface. Both ends of the anvil, BR, and BP were carefully polished using 1 μm diamond paste to enhance mechanical contact.

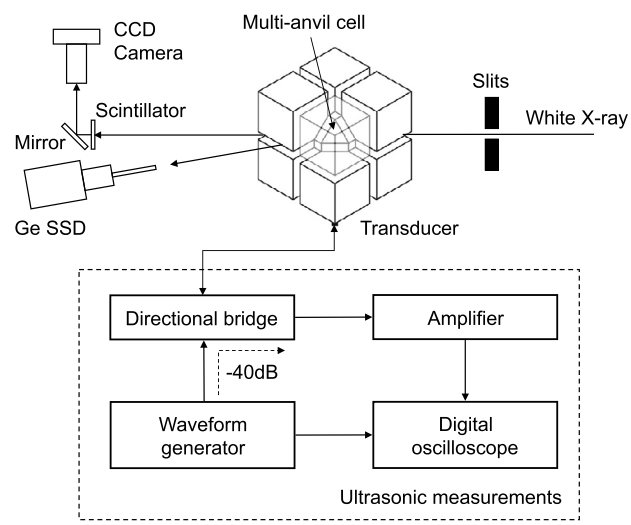

Fig. 2. Schematic drawing of the experimental setup for *in situ* ultrasonic sound velocity measurements at high pressures.

Fig. 2 shows the experimental setup for *in situ* ultrasonic measurements on liquids. We attached a 10° Y-cut $LiNbO_3$ piezoelectric transducer to the back of the WC anvil using high temperature epoxy resin. The resonant frequency of the transducer is 50 MHz for compressional waves (P-waves) and 30 MHz for shear waves (S-waves). Electrical signals of sine waves of 20–60 MHz (3–5 cycles) with $V_{\text{peak-to-peak}}$ of 1–5 V were generated by an arbitrary waveform generator and were converted to P and S waves by the transducer. Elastic waves propagated through the anvil, BR, and sample and were reflected back at the anvil-BR, BR-sample, and sample-BP interfaces. The reflected elastic waves were converted back to electrical signals by the transducer, amplified by a 40 dB pre-amplifier with a bandwidth of 0.2–40 MHz, and captured by a digital oscilloscope at a sampling rate of 5×10^9 sample/s. A directional bridge was used to avoid the damage to the oscilloscope by the high amplitude of the input signal. A high rpm cooling fan was used during the experiments to prevent overheating of the transducer.

Fig. 3a shows an example of compressional waves received at the digital oscilloscope for a liquid Fe–S sample. The two-way travel time for the sound waves propagating through the sample can be determined by the time difference between the arrivals of

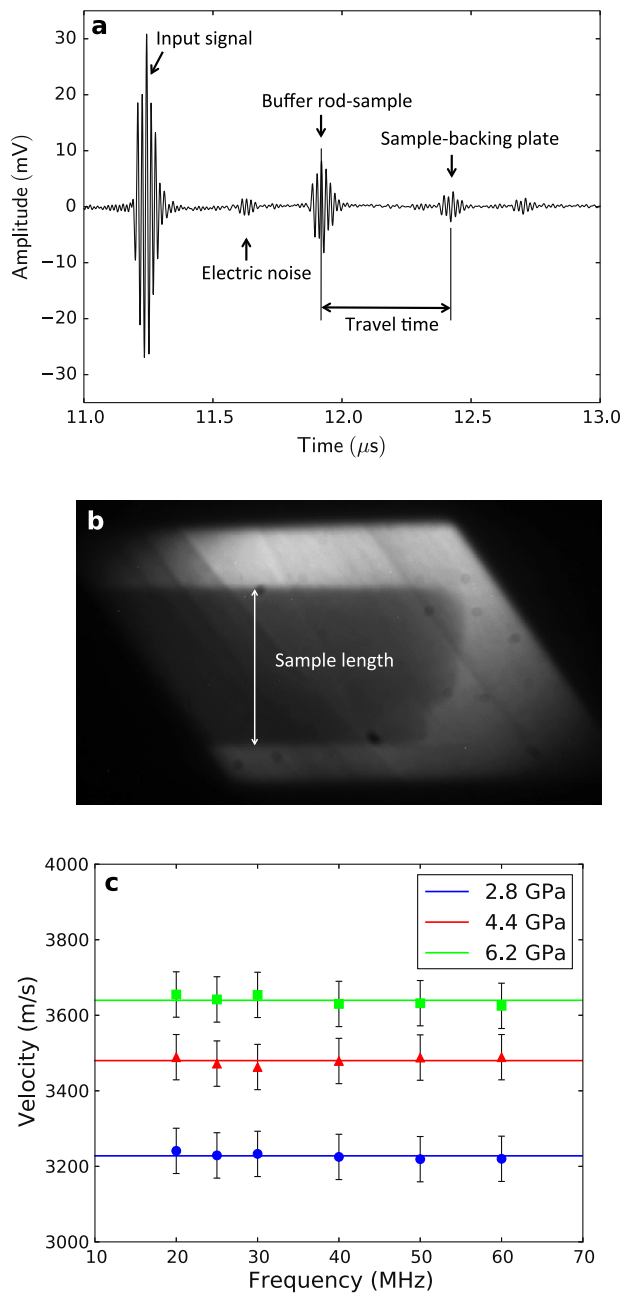

Fig. 3. (a) Compressional wave signals obtained for Fe–20S liquid at 2.7 GPa and 1573 K. There is a phase inversion at the sample-BP interface due to the higher impedance of Al_2O_3 than that of the sample. (b) X-ray radiographic image for the Fe–20S liquid sample at 2.7 GPa and 1573 K. (c) Sound velocities of Fe–20S liquids determined at various frequencies. Velocity results at 2.8, 4.4, and 6.2 GPa and 1673 K are shown. Horizontal lines represent the velocities averaged over the whole frequency range.

the echoes from the BR-sample interface and the sample-BP interface by the pulse-echo overlap method (Kono et al., 2012). Sample lengths were determined from the synchrotron X-ray radiographic images (Kono et al., 2012). A thin YAG crystal was used to convert X-ray intensity into visible light. A CCD camera was used to record images. Fig. 3b shows an example X-ray radiographic image for a liquid Fe–S sample. The uncertainties in sound velocities came mainly from the uncertainties in sample length measurements and were estimated to be about 2%.

We conducted velocity measurements on four different liquid compositions, including pure Fe, Fe–10 wt% S alloy (hereafter denoted as Fe–10S), Fe–20S, and Fe–27S. Fe and Fe–S samples were prepared by mixing appropriate amounts of reagent grade (99.9%) powders of Fe and FeS_2 (pyrite). Pure Fe and Fe–FeS_2 mixtures were ground with ethanol in an agate mortar for 1–2 h. Before experiments, sample materials were cold-pressed into pellets of ∼2 mm in diameter and ∼1.4 mm in height to ensure flatness and parallelism of the top and bottom surfaces. For each liquid composition, sound velocities were determined at three to five different fixed ram loads corresponding to various pressures from 1 to 8 GPa, at several temperatures ranging from ∼1573 K to ∼1973 K. Pressure standard was made from MgO and BN mixture (MgO:BN = 4:1 by weight). Pressure of the experiments was obtained by energy-dispersive X-ray diffraction of the MgO using the equation of state (EOS) determined by Tange et al. (2009). Temperature of the experiments was calculated based on the power-temperature relationship at each load calibrated using a W5Re–W26Re thermocouple in pilot experiments using exactly the same cell assemblies. The uncertainties in pressure and temperature are about 0.5 GPa and 100 K, respectively.

Complete melting of the sample was unequivocally identified by (1) the dramatic increase in the amplitude of the sound wave signals of the sample due to the disappearance of the scattering by partially molten materials, (2) the vanishing of shear waves propagating through the sample, (3) the significant delay of the P-wave travel time due to the low velocity of liquids, and (4) the disappearance of sample X-ray diffraction peaks and the appearance of diffused scattering of X-ray by the molten sample.

It is critical to make sure the measured sound velocities of liquids are fully relaxed, so that the measurements can be compared with seismic velocities directly. This is essentially ensured by the very low viscosities (η) of Fe and Fe–S liquids (in the range of 0.001–0.1 Pa s, Dobson et al., 2000; Terasaki et al., 2006). The estimated ambient-pressure bulk modulus (K) from static and shock-wave experiments is in the range of 10–100 GPa for Fe and Fe–S liquids (Anderson and Ahrens, 1994; Sanloup et al., 2000). The relaxation time, estimated by the relation $\tau \sim \eta/K$ (Herzfeld and Litovitz, 1959), is less than 0.01 ns. This means that a frequency of less than $0.01/\tau = 1$ GHz for the ultrasonic waves should give relaxed results. Also, in order to determine the travel time, the overlap of the BR-sample and sample-BP echoes must be avoided. This requires that the wavelength of the sound wave should be smaller than the length of the sample, which is on the order of 500 μm. Given a sound speed of ∼3000 m/s, the frequency of the ultrasonic waves should be higher than about 6 MHz. In this study, we applied various frequencies including 20 MHz, 25 MHz, 30 MHz, 40 MHz, 50 MHz, and 60 MHz to examine frequency dependence of velocity. As shown in Fig. 3c, the sound velocities determined are independent of frequency, indicating that the velocities are fully relaxed.

3. Results

Our velocity data are shown in Fig. 4 and Table 1. Overall, sound velocities increase upon compression, decrease with increasing sulfur content, and are nearly independent of temperature. For Fe and Fe–10S liquids, our results are consistent with previous measurements at ambient pressure (Fig. 4) (Hixson et al., 1990; Nasch et al., 1997).

We characterize the temperature dependence of sound velocity (c) using the adiabatic Anderson–Grüneisen parameter (Stacey, 2005),

$$\delta_S \equiv \left(\partial \ln(\alpha T/C_P)/\partial \ln V\right)_S = -(\partial \ln K_S/\partial T)_P/\alpha$$
$$= 1 - 2(\partial \ln c/\partial T)_P/\alpha, \quad (1)$$

where T is temperature, α the thermal expansion coefficient, and K_S the adiabatic bulk modulus. Using an α value of 1.3×10^{-4} K^{-1}

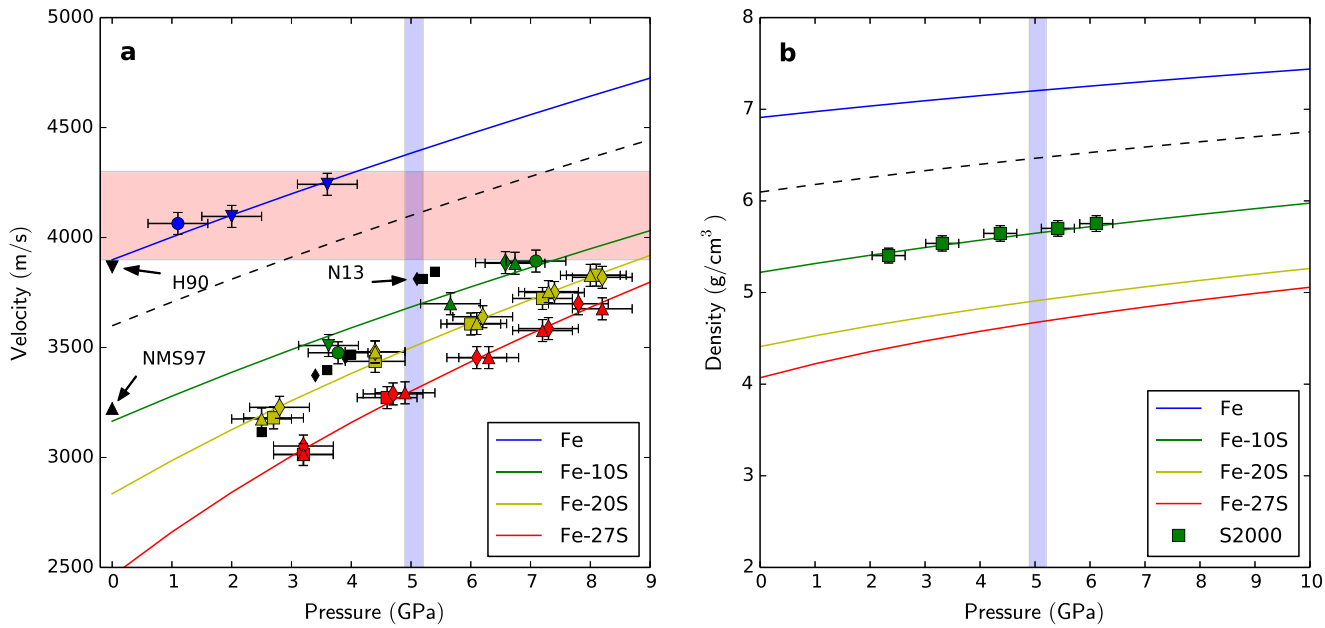

Fig. 4. Sound velocity and density of Fe–S liquids at high pressures. (a) Sound velocities measured at high pressures for pure Fe (blue), Fe–10S (green), Fe–20S (yellow), and Fe–27S (red). Temperature conditions of the measurements are represented by different symbols: 1573 K (squares), 1673 K (diamonds), 1773 K (up-pointing triangles), 1873 K (circles), and 1973 K (down-pointing triangles). The black down-pointing and up-pointing triangles are the ambient-pressure velocities for liquid Fe from Hixson et al. (1990) and liquid Fe–5Ni–10S from Nasch et al. (1997), respectively. The black squares and diamonds are velocities for liquid Fe–30S from Nishida et al. (2013). Error bars represent an uncertainty of 0.5 GPa in pressure and a relative uncertainty of 2% in velocity measurements. Solid curves with the same color-coding for liquid composition are calculated velocity profiles along the adiabat with a potential temperature of 1673 K using Eq. (5). The red shaded area represents the seismic velocity of the lunar outer core estimated from seismic data (Weber et al., 2011). (b) Density of Fe and Fe–S liquids at high pressures calculated using Eq. (4) and the parameters listed in Table 2, represented by the curves with the same color-coding as in (a). Green squares are density data for Fe–10S liquid from static measurements (Sanloup et al., 2000). In both (a) and (b), the vertical shaded bar represents the pressure of the lunar outer core (Garcia et al., 2011, 2012). The dashed curves are the calculated velocity (in a) and density (in b) profiles, respectively, for the Fe–4S liquid, the liquid that intersects the seismic-estimated outer core properties (i.e., the intersection of shaded blue and red areas in (a)). (For interpretation of the references to color in this figure legend, the reader is referred to the web version of this article.)

[α was estimated to be 1.3×10^{-4} K^{-1} for liquid Fe (Williams, 2009) and 1.5×10^{-4} K^{-1} for liquid Fe–36S (Kaiura and Toguri, 1979) at ambient pressure], the calculated $(\partial \ln c/\partial T)_P$ is $-(10 \pm 6) \times 10^{-5}$ K^{-1} for Fe–10S, $(2 \pm 2) \times 10^{-5}$ K^{-1} for Fe–20S, and $-(5 \pm 3) \times 10^{-5}$ K^{-1} for Fe–27S. This suggests that for Fe–S alloying liquids, $(\partial \ln c/\partial T)_P$ is close to zero given the uncertainties in velocity, and therefore $\delta_S = 1^{+1.5}_{-0.3}$. Similar temperature insensitivity of velocity was reported for Fe–30S liquid at high pressures (Nishida et al., 2013) and for Fe–5Ni–10S at ambient pressure (Nasch et al., 1997), although in the latter case the velocity increases slightly with temperature ($(\partial \ln c/\partial T)_P = 6 \times 10^{-5}$ K^{-1}). In contrast, the velocity of liquid Fe decreases with increasing temperature as demonstrated by ambient-pressure measurements (Hixson et al., 1990), yielding a δ_S of ~4, which was also hinted by our results at high pressures. The small δ_S for Fe–S liquids is likely due to the presence of sulfur, which drastically breaks the local structure of metallic Fe (Sanloup et al., 2002) and increases the entropy of the liquid. Contribution of such entropy to compression has been attributed to cause small δ_S in silicate liquids (Jing and Karato, 2011).

Compared to volumetric compression data, sound velocity data provide tight constraints on the bulk modulus and its pressure derivative of Fe and Fe–S liquids, and hence the equations of state of these liquids. The adiabatic bulk modulus can be obtained from the density (ρ) and sound velocity (c) as

$$K_S = \rho c^2. \tag{2}$$

In the small pressure range of this work (1–8 GPa), bulk moduli of Fe-rich liquids can be satisfactorily expressed by a linear function of pressure, that is,

$$K_S = K_{S0} + K'_S P, \tag{3}$$

where $K'_S = (\partial K_S/\partial P)_S$ is the pressure derivative of bulk modulus along isentropes and is a constant of pressure. Integration of Eq. (3) with respect to P gives the adiabatic Murnaghan EOS (Murnaghan, 1967)

$$\rho = \rho_0 \left(1 + \frac{K'_S}{K_{S0}} P\right)^{1/K'_S}. \tag{4}$$

Substituting Eqs. (3) and (4) into Eq. (2), we obtain the velocity as a function of pressure

$$c = \sqrt{\frac{K_{S0}}{\rho_0}} \left(1 + \frac{K'_S}{K_{S0}} P\right)^{\frac{1}{2} - \frac{1}{2K'_S}}, \tag{5}$$

with three EOS parameters ρ_0, K_{S0}, and K'_S to be determined by experimental data. Using Eq. (5), K_{S0}, and K'_S can be precisely determined by the ultrasonic sound velocity data if ρ_0 is known. In this study, we interpolated the results from previous density measurements on Fe and Fe–S liquids performed at ambient pressure (Hixson et al., 1990; Kaiura and Toguri, 1979; Sanloup et al., 2000) to set anchoring points for Eq. (5) with a potential temperature of 1673 K for the isentrope. The estimated ρ_0 and fitted results of K_{S0}, and K'_S are listed in Table 2.

The computed velocity and density at high pressures along the adiabat (equivalent to an isentrope for hydrostatic compression) with a potential temperature of 1673 K (the temperature of the adiabat at ambient pressure), using Eqs. (4) and (5) and parameters in Table 2, are shown in Fig. 4. The velocity data can be well explained by the Murnaghan EOS. Our calculated density for Fe–10S liquid is in good agreement with the density data obtained from static measurements at high pressures (Sanloup et al., 2000), further confirming that our measured velocities are fully relaxed and can be compared with seismic velocities directly. The fitted

Table 1
Experimental conditions and results of sound velocity measurements.

Sample	Run#	P (GPa)[a]	T (K)[b]	Frequency (MHz)	Velocity c (m/s)	Average c (m/s)	Standard deviation (m/s)
Fe	PE28	1.1	1873	25	4067	4064	11
Fe	PE28	1.1	1873	25	4053		
Fe	PE28	1.1	1873	30	4062		
Fe	PE28	1.1	1873	30	4056		
Fe	PE28	1.1	1873	40	4080		
Fe	PE28	2.0	1973	20	4112	4096	22
Fe	PE28	2.0	1973	25	4070		
Fe	PE28	2.0	1973	30	4104		
Fe	PE28	3.6	1973	30	4242	4242	0
Fe–10S	T1256	3.8	1873	20	3486	3476	10
Fe–10S	T1256	3.8	1873	25	3475		
Fe–10S	T1256	3.8	1873	30	3466		
Fe–10S	T1256	3.6	1973	20	3517	3509	10
Fe–10S	T1256	3.6	1973	25	3502		
Fe–10S	T1256	5.7	1773	20	3700	3699	2
Fe–10S	T1256	5.7	1773	25	3697		
Fe–10S	T1256	6.6	1673	20	3896	3886	13
Fe–10S	T1256	6.6	1673	25	3877		
Fe–10S	T1256	6.7	1773	20	3883	3883	2
Fe–10S	T1256	6.7	1773	25	3882		
Fe–10S	T1256	6.7	1773	30	3885		
Fe–10S	T1256	7.1	1873	20	3893	3893	0
Fe–20S	T1251	2.7	1573	20	3175	3180	8
Fe–20S	T1251	2.7	1573	25	3174		
Fe–20S	T1251	2.7	1573	30	3175		
Fe–20S	T1251	2.7	1573	40	3178		
Fe–20S	T1251	2.7	1573	50	3188		
Fe–20S	T1251	2.7	1573	60	3192		
Fe–20S	T1251	2.8	1673	20	3241	3228	8
Fe–20S	T1251	2.8	1673	25	3229		
Fe–20S	T1251	2.8	1673	30	3233		
Fe–20S	T1251	2.8	1673	40	3225		
Fe–20S	T1251	2.8	1673	50	3219		
Fe–20S	T1251	2.8	1673	60	3220		
Fe–20S	T1251	2.5	1773	20	3174	3175	14
Fe–20S	T1251	2.5	1773	25	3167		
Fe–20S	T1251	2.5	1773	30	3150		
Fe–20S	T1251	2.5	1773	40	3187		
Fe–20S	T1251	2.5	1773	50	3187		
Fe–20S	T1251	2.5	1773	60	3186		
Fe–20S	T1251	4.4	1573	20	3423	3437	19
Fe–20S	T1251	4.4	1573	25	3422		
Fe–20S	T1251	4.4	1573	30	3417		
Fe–20S	T1251	4.4	1573	40	3443		
Fe–20S	T1251	4.4	1573	50	3459		
Fe–20S	T1251	4.4	1573	60	3458		
Fe–20S	T1251	4.4	1673	20	3489	3480	11
Fe–20S	T1251	4.4	1673	25	3472		
Fe–20S	T1251	4.4	1673	30	3463		
Fe–20S	T1251	4.4	1673	40	3479		
Fe–20S	T1251	4.4	1673	50	3488		
Fe–20S	T1251	4.4	1673	60	3489		
Fe–20S	T1251	4.4	1773	20	3491	3480	14
Fe–20S	T1251	4.4	1773	25	3462		
Fe–20S	T1251	4.4	1773	30	3468		
Fe–20S	T1251	4.4	1773	40	3474		
Fe–20S	T1251	4.4	1773	50	3491		
Fe–20S	T1251	4.4	1773	60	3494		
Fe–20S	T1251	6.0	1573	20	3594	3607	21
Fe–20S	T1251	6.0	1573	25	3622		
Fe–20S	T1251	6.0	1573	30	3584		
Fe–20S	T1251	6.0	1573	40	3628		
Fe–20S	T1251	6.2	1673	20	3655	3640	13
Fe–20S	T1251	6.2	1673	25	3642		
Fe–20S	T1251	6.2	1673	30	3654		
Fe–20S	T1251	6.2	1673	40	3630		
Fe–20S	T1251	6.2	1673	50	3632		
Fe–20S	T1251	6.2	1673	60	3625		
Fe–20S	T1251	6.1	1773	20	3612	3609	5
Fe–20S	T1251	6.1	1773	25	3599		
Fe–20S	T1251	6.1	1773	30	3611		
Fe–20S	T1251	6.1	1773	40	3606		
Fe–20S	T1251	6.1	1773	50	3611		
Fe–20S	T1251	6.1	1773	60	3612		

Table 1 (*continued*)

Sample	Run#	P (GPa)[a]	T (K)[b]	Frequency (MHz)	Velocity c (m/s)	Average c (m/s)	Standard deviation (m/s)
Fe–20S	T1251	7.2	1573	20	3722	3723	4
Fe–20S	T1251	7.2	1573	25	3719		
Fe–20S	T1251	7.2	1573	30	3727		
Fe–20S	T1251	7.4	1673	20	3752	3750	4
Fe–20S	T1251	7.4	1673	25	3752		
Fe–20S	T1251	7.4	1673	30	3745		
Fe–20S	T1251	7.3	1773	20	3753	3754	11
Fe–20S	T1251	7.3	1773	25	3747		
Fe–20S	T1251	7.3	1773	30	3742		
Fe–20S	T1251	7.3	1773	40	3750		
Fe–20S	T1251	7.3	1773	50	3760		
Fe–20S	T1251	7.3	1773	60	3772		
Fe–20S	T1251	8.1	1573	20	3820	3829	6
Fe–20S	T1251	8.1	1573	25	3829		
Fe–20S	T1251	8.1	1573	30	3835		
Fe–20S	T1251	8.1	1573	40	3832		
Fe–20S	T1251	8.2	1673	20	3818	3819	2
Fe–20S	T1251	8.2	1673	30	3821		
Fe–20S	T1251	8.0	1773	20	3815	3828	19
Fe–20S	T1251	8.0	1773	25	3841		
Fe–27S	T1254	3.2	1573	20	3008	3014	8
Fe–27S	T1254	3.2	1573	25	3009		
Fe–27S	T1254	3.2	1573	30	3013		
Fe–27S	T1254	3.2	1573	40	3026		
Fe–27S	T1254	3.2	1673	20	3050	3052	8
Fe–27S	T1254	3.2	1673	25	3061		
Fe–27S	T1254	3.2	1673	30	3046		
Fe–27S	T1254	3.2	1773	20	3011	3013	2
Fe–27S	T1254	3.2	1773	25	3013		
Fe–27S	T1254	3.2	1773	30	3015		
Fe–27S	T1254	4.6	1573	20	3266	3272	6
Fe–27S	T1254	4.6	1573	25	3271		
Fe–27S	T1254	4.6	1573	30	3279		
Fe–27S	T1254	4.7	1673	20	3293	3289	8
Fe–27S	T1254	4.7	1673	25	3280		
Fe–27S	T1254	4.7	1673	30	3296		
Fe–27S	T1254	4.9	1773	20	3302	3294	8
Fe–27S	T1254	4.9	1773	25	3287		
Fe–27S	T1254	4.9	1773	30	3292		
Fe–27S	T1254	6.1	1673	20	3461	3454	9
Fe–27S	T1254	6.1	1673	25	3456		
Fe–27S	T1254	6.1	1673	30	3445		
Fe–27S	T1254	6.3	1773	20	3466	3454	16
Fe–27S	T1254	6.3	1773	25	3460		
Fe–27S	T1254	6.3	1773	30	3437		
Fe–27S	T1254	7.3	1673	20	3574	3586	11
Fe–27S	T1254	7.3	1673	25	3597		
Fe–27S	T1254	7.3	1673	30	3587		
Fe–27S	T1254	7.2	1773	20	3582	3577	6
Fe–27S	T1254	7.2	1773	25	3578		
Fe–27S	T1254	7.2	1773	30	3570		
Fe–27S	T1254	7.8	1673	20	3720	3699	19
Fe–27S	T1254	7.8	1673	25	3694		
Fe–27S	T1254	7.8	1673	30	3683		
Fe–27S	T1254	8.2	1773	20	3694	3676	26
Fe–27S	T1254	8.2	1773	25	3658		

[a] Uncertainties in pressure are about 0.5 GPa.
[b] Temperatures were estimated from the power-temperature relationship calibrated by a pilot experiment using the same cell assembly and run procedure. Uncertainties in temperature are about 100 K.

ambient-pressure bulk modulus K_{S0} decreases with increasing sulfur content (Table 2), while K'_S for all liquids studied are in the range of 4.9 to 6.7. The sound velocity results for Fe–S liquids are not to be extrapolated to pressures greater than 13–17 GPa, where sulfur in liquid Fe becomes increasingly metallic (Morard et al., 2007).

4. Discussion

4.1. Comparison with the results of Nishida et al. (2013)

Extrapolation of our results for Fe–27S to slightly higher sulfur content (Fe–30S) suggests lower velocities and significantly smaller pressure effect on velocity than the results of Nishida et al. (2013) (Fig. 4a). The reason for the discrepancies between our data and those of Nishida et al. (2013) is unknown. A difference in experimental procedures is that our measurements for each liquid composition at various pressure and temperature conditions were carried out on the same sample in a single experiment through multiple heating cycles at different ram loads, whereas velocity data in Nishida et al. (2013) at different pressures were obtained from multiple experiments. Therefore the relative errors between velocity measurements at different pressures and temperatures were minimized in our study.

Sound velocities of liquid Fe–30S determined by Nishida et al. (2013) increase dramatically with increasing pressure and would

Table 2
Fitted parameters based on the Murnaghan EOS.

Composition	ρ_0 (g/cm^3)[a]	K_{S0} (GPa)	K'_S
Fe	6.91	105 (2)	6.7 (1.0)
Fe–10S	5.22	52 (2)	4.9 (0.4)
Fe–20S	4.41	35 (1)	4.9 (0.1)
Fe–27S	4.07	25 (1)	5.3 (0.1)

[a] Ambient-pressure densities (ρ_0) for Fe and Fe–10S at 1673 K are from Hixson et al. (1990) and Sanloup et al. (2000), respectively. ρ_0 for Fe–20S and Fe–27S at 1673 K are interpolated from ρ_0 of Fe, Fe–10S, and Fe–36S from Hixson et al. (1990), Kaiura and Toguri (1979), and Sanloup et al. (2000).

surpass the velocity of liquid Fe at about 7 GPa. Nishida et al. (2013) found a linear relationship between velocity and pressure, i.e., $c = a + bP$, with $a = 2470.4$ (m/s) and $b = 257.21$ (ms^{-1} GPa^{-1}). Using this relationship and noticing that $K_S = \rho(\partial P/\partial\rho)_S = \rho c^2$, one can obtain the density and bulk modulus as functions of pressure as $\rho = \rho_0 + \frac{1}{b}(\frac{1}{a} - \frac{1}{a+bP})$ and $K_S = (\rho_0 + \frac{1}{ab})(a+bP)^2 - \frac{1}{b}(a+bP)$, where ρ_0 is the ambient-pressure density and is about 4.0 g/cm^3 for liquid Fe–30S. K'_S can also be obtained by taking the pressure derivative of K_S, which yields $K'_S = 6.1 + 0.74 \times P$ (GPa). The positive linear relationship between K'_S and P indicates that liquid Fe–30S quickly becomes nearly incompressible at relatively low pressures. In fact, as pressure goes to infinity, there exists a density limit for the liquid: $\rho_\infty = \rho_0 + \frac{1}{ab} = 5.6$ g/cm^3. This means the maximum density increase that can be achieved from the ambient-pressure density is only about 40%. However, shockwave data (e.g., Huang et al., 2011) show that the density of Fe-rich liquids can be 60–100% higher than the ambient-pressure density under Earth's outer core conditions, and even with such high degree of compression, the shockwave data do not show any asymptotic density limit. In contrast to Nishida et al. (2013), our velocity data show similar pressure dependencies for Fe–S and Fe liquids (similar K'_S values, Table 2) and are consistent with the shockwave data on liquid Fe ($K'_S = 4.7$, Anderson and Ahrens, 1994).

4.2. Sulfur content, density, and temperature of the lunar outer core

We examined the effect of sulfur on lunar outer core properties by fitting the velocity and density results for the four liquid compositions at 5 GPa to quadratic functions of sulfur mole fraction, respectively (Figs. 5a and 5b). Compared to the velocity in the outer core estimated from lunar seismic data (Weber et al., 2011), a sulfur content of ~3.6 wt% is required to reduce the velocity of pure liquid Fe to the outer core velocity of ~4100 m/s. This sulfur content corresponds to a density of ~6.5 g/cm^3 for the outer core, which is significantly higher than the estimate of 5.1 g/cm^3 obtained by Weber et al. (2011) based on volumetric compression data (Balog et al., 2003; Sanloup et al., 2000) for both density and velocity estimation, and the estimation of 5.2 g/cm^3 for the entire core by Garcia et al. (2011), derived from a core radius of 380 km.

The uncertainty in the seismic velocity of the outer core is the major source of error for the estimated outer core properties. For a 90-km thick outer core (Weber et al., 2011), the two-way travel time for seismic waves propagating through the outer core (reflected back at the inner-core boundary) is about 44 seconds, assuming a velocity of 4100 m/s. Given the minimum stacking time window of 2 seconds in Weber et al. (2011), we estimated the uncertainty in travel time to be about 5%, which converted to an uncertainty of 200 m/s in velocity. Such an uncertainty in the outer core velocity corresponds to uncertainties of ~3 wt% in sulfur content and ~0.5 g/cm^3 in density. The presence of nickel in the liquid core does not modify our conclusion on the sulfur content, since liquid Ni has a velocity close to that of liquid Fe (Hixson et al., 1990), although it would mean a slightly higher core density (Hixson et al., 1990). With 10 wt% Ni in the outer core, the estimated core density would be ~1% higher. On the other hand, the presence of other light elements such as silicon and oxygen would require higher sulfur content as these elements increase the velocity of liquid Fe, in contrast to sulfur (Huang et al., 2011; Sanloup et al., 2004), and, consequently, a lower outer core density.

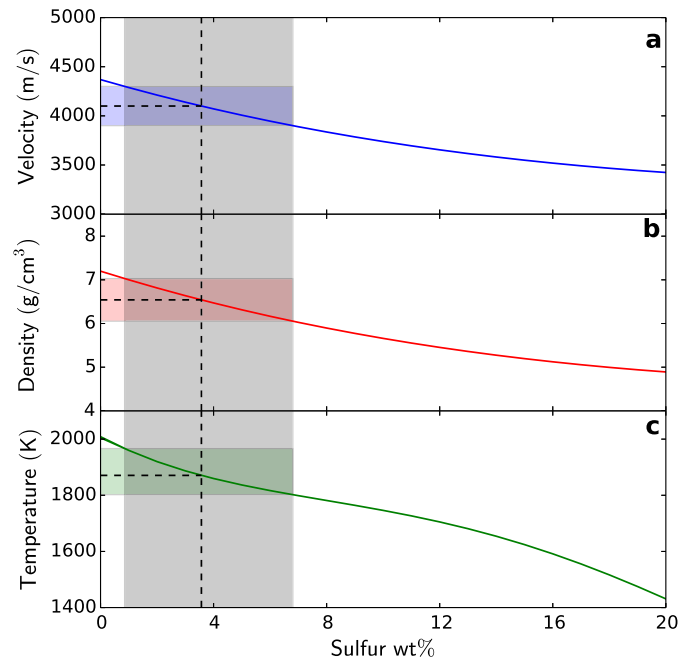

Fig. 5. Effects of sulfur on the properties of Fe–S liquids. (a) Effect of sulfur on the velocity of Fe–S liquids at 5 GPa. The seismic velocity of the lunar outer core estimated by Weber et al. (2011) (4100 ± 200 m/s) is shown as the blue shaded area. The gray shaded area is the estimated sulfur content required to reduce the velocity of Fe-rich liquids to 4100 m/s. (b) Effect of sulfur on the density of Fe–S liquids at 5 GPa. (c) Liquidus of the Fe–S binary system at 5 GPa. The estimated density and temperature of the lunar outer core are represented by the red and green shaded areas in (b) and (c), respectively. (For interpretation of the references to color in this figure legend, the reader is referred to the web version of this article.)

Thermodynamically, the equilibrium sulfur content as a function of core temperature is defined by the liquidus of the Fe–S binary system. During cooling of the lunar core, solid Fe likely precipitated out of the liquid outer core, increasing the sulfur content in the liquid. Fig. 5c shows the binary phase diagram of the Fe–S system at 5 GPa interpolated from the results determined at ambient-pressure (Hansen and Anderko, 1958), 3 GPa (Brett and Bell, 1969), 6 GPa (Buono and Walker, 2011), and 10 GPa (Chen et al., 2008). Given a sulfur content of 3.6 wt% for the outer core, we estimated the temperature of the lunar outer core to be 1870^{+100}_{-70} K (Fig. 5c).

This temperature is high enough to support a partially molten silicate layer at the bottom of the lunar mantle, consistent with seismological observations (Weber et al., 2011). Such a deep partial melt layer is likely gravitationally stable due to the large compressibility of the melt and the presence of the denser TiO_2 component in the melt (van Kan Parker et al., 2012).

4.3. Core size and the internal structure of the Moon

We employed the total mass $M = 7.3477 \times 10^{22}$ kg (Konopliv et al., 2001; Wieczorek et al., 2006) and the mean moment of inertia ratio $I = 0.3935$ (Konopliv et al., 1998; Wieczorek et al., 2006) to place constraints on the core size and the internal structure of the Moon. We assumed a four-layer structure containing crust, mantle, outer core, and inner core. The inner core density

was calculated to be 7.75 g/cm^3 from the EOS of face-centered cubic phase (γ phase) of iron (Komabayashi and Fei, 2010) at 5.5 GPa and 1870 K. The outer core density was given as 6.5 g/cm^3 from this study. We assumed an outer core thickness of 90 km, to be consistent with the seismic velocity of 4100 m/s (Weber et al., 2011) (there is a one-to-one tradeoff between the layer thickness and layer velocity as they were determined from travel time). Recent results from the Gravity Recovery and Interior Laboratory (GRAIL) mission (Wieczorek et al., 2013) provided four different lunar crust models with two possible crust densities (2.55 g/cm^3 or 2.70 g/cm^3) depending on the porosity of the entire crust and two possible thicknesses (35 km or 43 km) depending on the seismically determined crust thicknesses near the Apollo 12 and 14 landing sites. The density of the uppermost mantle was also constrained for each crust model by the gravity data. We applied the crust density and thickness from each model of Wieczorek et al. (2013) to constrain the core size and mantle density.

The density of the mantle was modeled using the Murnghan EOS (Eq. (4)) with the ambient-pressure density (ρ_0^{m}) of the mantle material as a free parameter, assuming the lunar mantle is homogeneous and follows an adiabatic temperature gradient (see Appendix A). The adiabatic assumption may not be valid in the upper part of the mantle (Gagnepain-Beyneix et al., 2006), but the deviation from adiabatic temperature should not contribute much to the uncertainties in core size as the dominating factor would be the large density difference between the outer core and the mantle. The bulk modulus (K_{S0}^{m}) of the mantle was estimated from the longitudinal and shear velocities of the uppermost mantle ($V_P = 7.65 \pm 0.06$ km/s, $V_S = 4.44 \pm 0.04$ km/s) (Gagnepain-Beyneix et al., 2006) by $K_S^{\mathrm{m}} = \rho^{\mathrm{m}}(V_P^2 - \frac{4}{3}V_S^2)$. For the likely density range of 3.3–3.35 g/cm^3 for the uppermost mantle (will be shown below), K_{S0}^{m} is estimated to be 107 ± 5 GPa. The pressure derivative of K_{S0}^{m} (K_{S0}^{m}) is assumed to be 4, which is a typical value for mantle materials (Stixrude and Lithgow-Bertelloni, 2005). The core radius (r_{oc}), the other free parameter of the model, is incorporated as the boundary condition for the mantle density model at the lunar core-mantle boundary (Appendix A). Therefore two constraints, mass and moment of inertia ratio, were used to solve two unknowns, the uppermost mantle density (ρ_0^{m}) and the core radius (r_{oc}).

For the two crust models with a crust density of 2.55 g/cm^3, our calculated uppermost mantle densities are 3.32 and 3.35 g/cm^3, which are much higher than the mantle densities of 3.22 g/cm^3 and 3.15 g/cm^3 constrained by the gravity data for these two models (Wieczorek et al., 2013). We therefore ruled out these two cases. For the two models with a crust density of 2.70 g/cm^3, out calculated core radius and uppermost mantle density are, respectively, 290 km and 3.32 g/cm^3 for a 35 km thick crust, and 250 km and 3.33 g/cm^3 for a 43 km thick crust, consistent with the uppermost mantle densities of 3.36 g/cm^3 and 3.30 g/cm^3 from the gravity data (Wieczorek et al., 2013) for these two models. The difference between the results of the latter two models reflects a trade-off of mass distribution between the core, mantle, and crust under the mass and moment of inertia constraints. Our preferred core size is 290 km as it is consistent with the estimate by electromagnetic sounding using lunar satellites data (Shimizu et al., 2013), but there is no reason to reject the possibility of a 250 km radius core using the constraints applied in this study. Both results are significantly smaller than the 380 km result obtained by Garcia et al. (2011). An uncertainty of 0.5 g/cm^3 in outer core density would only result in a 10-km uncertainty in core size. The uncertainty in outer core thickness has an even smaller effect due to the similar densities of the inner and outer cores. The uncertainty in core size caused by a 5% uncertainty in the outer core thickness is less than 1 km. The preferred internal structure model of the Moon is shown in Fig. 6. The

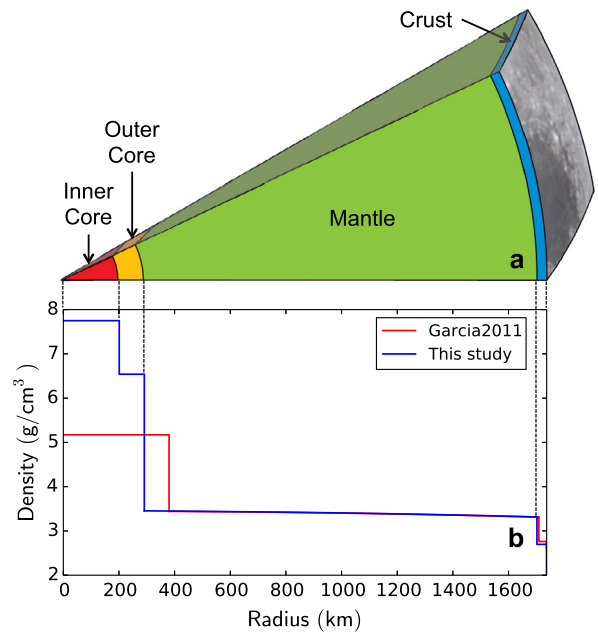

Fig. 6. Preferred internal structure model of the Moon. (a) Illustration of a four-layer structure model of the Moon, consisting of an inner core, an outer core, a mantle, and a crust. (b) The density profile of the Moon as a function of radius from this study is shown in blue. For comparison, the model from Garcia et al. (2011) is shown in red. (For interpretation of the references to color in this figure legend, the reader is referred to the web version of this article.)

assumed and calculated parameters of the model are listed in Table 3. For the preferred model, the calculated pressure is 4.9 GPa at the core mantle boundary, 5.2 GPa at the inner core boundary, and 5.6 GPa at the center of the Moon, consistent with the assumed outer core pressure of 5 GPa.

4.4. Solidification scheme of the lunar core

In a convecting liquid layer, the adiabatic temperature gradient can be calculated from the Anderson–Grüneisen parameter (Stacey, 2005) by integrating Eq. (1), yielding

$$\left(\frac{\partial T}{\partial P}\right)_S = \frac{\alpha T}{\rho C_P} = \left(\frac{\alpha_0 T_0}{\rho_0 C_{P0}}\right)\left(\frac{\rho_0}{\rho}\right)^{\delta_S+1}. \tag{6}$$

where C_P is the isobaric heat capacity, T_0 the potential temperature, and $\delta_S \sim 1$ for Fe–S liquids at high pressures. Assuming α_0 of the lunar core has a value between those of liquid Fe (1.3×10^{-4} K^{-1}) (Williams, 2009) and liquid Fe–36S (1.5×10^{-4} K^{-1}) (Kaiura and Toguri, 1979) and C_P is 835 J kg^{-1} K^1 (the liquid Fe value, Desai, 1986), the estimated adiabatic temperature gradient is ∼38–43 K/GPa. This slope is significantly larger than that of the Fe–S liquidus temperature as a function of pressure, which varies from ∼33 K/GPa for Fe (Boehler et al., 1986; Strong et al., 1973) to −34 K/GPa for Fe–20S (interpolated from the results of Hansen and Anderko, 1958; Brett and Bell, 1969; Buono and Walker, 2011, and Chen et al., 2008). Consequently, during the secular cooling of the Moon, solidification of the liquid Fe–S lunar core likely initiated from the top of the core and proceeded downwards (Fig. 7), similar to the Fe-snow scenario proposed for the cores of Ganymede (Hauck et al., 2006) and other small solar system bodies (Williams, 2009). The Fe "snow" would sink under gravity and re-melt at deeper parts of the core. The re-distribution of iron and sulfur in due process would lower the liquidus temperature at the top of the outer core (due to increasing sulfur content) and elevate that of the deep outer core (increasing Fe content). As the cooling process continues, the Fe snow zone

Table 3
Preferred parameters for the lunar internal structure model.

Parameter	Value[a]	Source
Radius of the Moon (km)	1737.1	Smith et al. (1997)
Mass (kg)	7.3477×10^{22}	Konopliv et al. (2001); Wieczorek et al. (2006)
Mean moment of inertia ratio	0.3935	Konopliv et al. (1998); Wieczorek et al. (2006)
Crust density (g/cm^3)	2.70	Wieczorek et al. (2013)
Crust thickness (km)	35 (43)	Wieczorek et al. (2013)
Density of upper most mantle (g/cm^3)	3.32 (3.33)	Fitted
K_S of upper most mantle (GPa)	107	Calculated from the V_P and V_S of the upper most mantle (Gagnepain-Beyneix et al., 2006)
K'_S of mantle	4	Assumed (Stixrude and Lithgow-Bertelloni, 2005)
Mantle thickness (km)	1412 (1444)	Derived
Outer core density (g/cm^3)	6.5	Calculated from the EOS of liquid Fe–4S of this work
Outer core thickness (km)	90	Weber et al. (2011)
Inner core density (g/cm^3)	7.75	Calculated from the EOS of γ-Fe (Komabayashi and Fei, 2010)
Inner core thickness (km)	200 (160)	Fitted

[a] Values in parentheses are for the model with a 43 km thick crust.

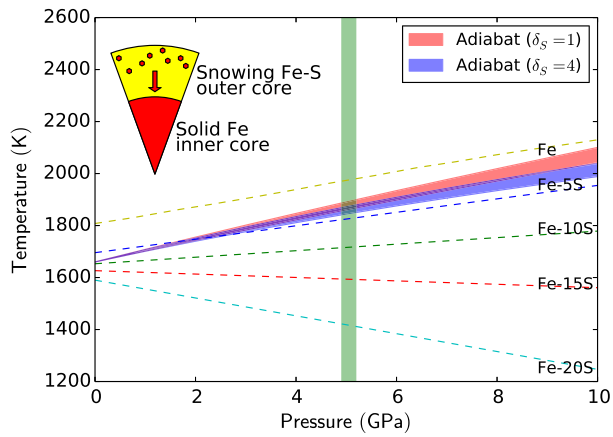

Fig. 7. Adiabatic temperature profile in the liquid outer core. The red shaded area represents the adiabatic temperature in liquid Fe–S calculated using $\delta_S = 1$ as indicated by our experimental data. For comparison, the blue shaded area shows the adiabatic temperature profile calculated using $\delta_S = 4$ (estimated value for liquid Fe). The lower and upper bounds of the shaded areas correspond to calculations using thermal expansion coefficients of 1.3×10^{-4} K^{-1} and 1.5×10^{-4} K^{-1}, respectively (Kaiura and Toguri, 1979; Williams, 2009). The potential temperature of the adiabats is chosen to be 1660 K in order to yield an outer core temperature of 1870 K for the $\delta_S = 1$ case. The dashed curves are the melting curve of pure Fe and interpolated liquidus temperatures for Fe–S alloys. The green shaded area represents the pressure of the lunar outer core. The slope of the adiabatic temperature profile for the lunar outer core is steeper than the liquidus curves, indicating that as the lunar core was cooled, Fe precipitation started from the top of the core. Solid Fe crystals would fall downwards under gravity, forming an Fe-snow as shown by the cartoon inset. (For interpretation of the references to color in this figure legend, the reader is referred to the web version of this article.)

broadens and eventually the liquidus of the outer core would become identical to the adiabat. Further cooling would precipitate Fe throughout the entire outer core, forming the solid inner core as Fe gravitationally sinks. This inner core forming process contrasts the growing inner core scenario in Earth (Buffett et al., 1992), and should be considered in modeling the thermochemically-driven early lunar dynamo (Stegman et al., 2003).

5. Conclusion

Sound velocities of pure Fe and three Fe–S liquids with 10, 20, and 27 wt% S were determined under high pressure–temperature conditions ranging from 1–8 GPa and 1573–1973 K. The measured velocities are independent of frequency and are consistent with the density data in the literature from static compression experiments, indicating that the velocities are fully relaxed and can be directly compared to seismic velocities. Our results show that the velocity of Fe-rich liquids increases with increasing pressure, decreases with increasing sulfur content, and is nearly independent of temperature. Comparing our velocity data to the lunar seismic model, the sulfur content in the outer core was constrained to be 4 ± 3 wt%. This sulfur content implies a denser and hotter outer core, and a smaller core radius than previously estimated. Our results also suggest that the solidification of the lunar outer core likely started from the top of the core, in contrast to the growing inner core scenario in Earth.

Acknowledgements

We thank C. Kenney-Benson and Ellen LaRue for their technical support and three anonymous reviewers for their constructive comments. This work was supported by the National Science Foundation (EAR-0711057, 1214376). Experiments were performed at the GSECARS beamline 13-ID-D and the HPCAT beamline 16-BM-B of the Advanced Photon Source (APS), Argonne National Laboratory. GSECARS is supported by the NSF EAR-0622171 and U.S. Department of Energy (DOE) DE-FG02-94ER14466. HPCAT is supported by DOE-NNSA under Award No. DE-NA0001974 and DOE-BES under Award No. DE-FG02-99ER45775, with partial instrumentation funding by NSF. The APS is supported by DOE Office of Science, Basic Energy Sciences, Contract No. DE-AC02-06CH11357.

Appendix A. Density distribution in the lunar mantle

The mantle density distribution as a function of radius r can be derived by

$$\frac{d\rho}{dr} = -\frac{\rho^2 G M_r}{K_S r^2}, \tag{A.1}$$

where G is gravity constant, and M_r is the mass enclosed within radius r given as

$$dM_r = 4\pi\rho r^2 dr. \tag{A.2}$$

Substituting Eqs. (3), (4), and (A.1) into Eq. (A.2), we obtain Emden's equation (Lyttleton, 1965)

$$\frac{d^2 y}{dx^2} + \frac{2}{x}\frac{dy}{dx} + y^\mu = 0, \tag{A.3}$$

where $\mu = 1/(K'_S - 1)$ is a constant, x and y are related to the radius and density as $x = A\mu^{-\mu/2} r$ and $y = \mu\rho^{1/\mu}$ with $A = (4\pi G \rho_0^{K'_S}/K_{S0})^{1/2}$. Two boundary conditions are given by the continuity of gravity at the core-mantle boundary ($r = r_{oc}$) and the crust-mantle boundary ($r = r_m$), as

$$\left.\frac{dy}{dx}\right|_{x=x_{oc}} = -\frac{A}{4\pi\mu^{-\mu/2}}\frac{M_{oc} + M_{ic}}{r_{oc}^2}, \tag{A.4}$$

$$\left.\frac{dy}{dx}\right|_{x=x_m} = -\frac{A}{4\pi\mu^{-\mu/2}}\frac{M - M_{cr}}{r_m^2}, \tag{A.5}$$

where r_{oc} and r_m are the outer radii of the outer core and mantle, M_{ic}, M_{oc}, and M_{cr} are the masses of the inner core, outer core, and crust, calculated from their densities and inner and outer radii respectively. These boundary conditions are equivalent to the total mass constraint. For a given r_{oc}, ρ_0^m is sought by integrating Eq. (A.3) to satisfy both boundary conditions Eqs. (A.4) and (A.5). This yields a relation between r_{oc} and ρ_0^m, and a mantle density distribution that depends on r_{oc} and ρ_0^m. The density distribution of the Moon must also satisfy the mean moment of inertia constraint

$$I = \frac{8\pi}{3} \int_0^R \rho r^4 \, dr, \tag{A.6}$$

where $R = 1737.1$ km is the radius of the Moon (Smith et al., 1997). Therefore, we have two constraints to solve for two unknown parameters r_{oc} and ρ_0^m.

References

Anderson, W.W., Ahrens, T.J., 1994. An equation of state for liquid iron and implications for the Earth's core. J. Geophys. Res. 99, 4273–4284.

Balog, P.S., Secco, R.A., Rubie, D.C., Frost, D.J., 2003. Equation of state of liquid Fe-10 wt% S: implications for the metallic cores of planetary bodies. J. Geophys. Res. 108, 2124. http://dx.doi.org/10.1029/2001JB001646.

Boehler, R., Nicol, M., Zha, C.S., Johnson, M.L., 1986. Resistance heating of Fe and W in diamond-anvil cells. Physica B 139–140, 916–918.

Brett, R., Bell, P.M., 1969. Melting relations in the Fe-rich portion of the system Fe–FeS at 30 kb pressure. Earth Planet. Sci. Lett. 6, 479–482.

Buffett, B.A., Huppert, H.E., Lister, J.R., Woods, A.W., 1992. Analytical model for solidification of the Earth's core. Nature 356, 329–331.

Buono, A.S., Walker, D., 2011. The Fe-rich liquidus in the Fe–FeS system from 1 bar to 10 GPa. Geochim. Cosmochim. Acta 75, 2072–2087.

Chabot, N., 2004. Sulfur contents of the parental metallic cores of magmatic iron meteorites. Geochim. Cosmochim. Acta 68, 3607–3618.

Chen, B., Li, J., Hauck II, S.A., 2008. Non-ideal liquidus curve in the Fe–S system and Mercury's snowing core. Geophys. Res. Lett. 35, L07201. http://dx.doi.org/10.1029/2008GL033311.

Desai, P.D., 1986. Thermodynamic properties of iron and silicon. J. Phys. Chem. Ref. Data 15, 967–983.

Dobson, D.P., Crichton, W.A., Vočadlo, L., Jones, A.P., Wang, Y., Uchida, T., Rivers, M.L., Sutton, S.R., Brodholt, J.P., 2000. In situ measurement of viscosity of liquids in the Fe–FeS system at high pressures and temperatures. Am. Mineral. 85, 1838–1842.

Gagnepain-Beyneix, J., Lognonné, P., Chenet, H., Lombardi, D., Spohn, T., 2006. A seismic model of the lunar mantle and constraints on temperature and mineralogy. Phys. Earth Planet. Inter. 159, 140–166.

Garcia, R.F., Gagnepain-Beyneix, J., Chevrot, S., Lognonné, P., 2011. Very preliminary reference Moon model. Phys. Earth Planet. Inter. 188, 96–113.

Garcia, R.F., Gagnepain-Beyneix, J., Chevrot, S., Lognonné, P., 2012. Erratum to "Very Preliminary Reference Moon Model", by R.F. Garcia, J. Gagnepain-Beyneix, S. Chevrot, P. Lognonné [Phys. Earth Planet. Inter. 188 (2011) 96–113]. Phys. Earth Planet. Inter. 202–203, 89–91.

Hansen, M., Anderko, K., 1958. Constitution of the Binary Alloys, 2nd ed. McGraw-Hill Book Co., New York.

Hauck, S.A., Aurnou, J.M., Dombard, A.J., 2006. Sulfur's impact on core evolution and magnetic field generation. J. Geophys. Res. 111, E09008. http://dx.doi.org/10.1029/2005JE002557.

Herzfeld, K.F., Litovitz, T.A., 1959. Absorption and Dispersion of Ultrasonic Waves. Academic Press.

Hixson, R.S., Winkler, M.A., Hodgdon, M.L., 1990. Sound speed and thermophysical properties of liquid iron and nickel. Phys. Rev. B 42, 6485–6491.

Huang, H., Fei, Y., Cai, L., Jing, F., Hu, X., Xie, H., Zhang, L., Gong, Z., 2011. Evidence for an oxygen-depleted liquid outer core of the Earth. Nature 479, 513–516.

Jing, Z., Karato, S., 2011. A new approach to the equation of state of silicate melts: an application of the theory of hard sphere mixtures. Geochim. Cosmochim. Acta 75, 6780–6802.

Kaiura, G.H., Toguri, J.M., 1979. Densities of the molten FeS, FeS–Cu_2S and Fe–S–O systems-utilizing a bottom-balance Archimedean technique. Can. Metall. Q. 18, 155–164.

Komabayashi, T., Fei, Y., 2010. Internally consistent thermodynamic database for iron to the Earth's core conditions. J. Geophys. Res. 115, B03202. http://dx.doi.org/10.1029/2009JB006442.

Kono, Y., Park, C., Sakamaki, T., Kenny-Benson, C., Shen, G., Wang, Y., 2012. Simultaneous structure and elastic wave velocity measurement of SiO_2 glass at high pressures and high temperatures in a Paris–Edinburgh cell. Rev. Sci. Instrum. 83, 033905.

Konopliv, A.S., Asmar, S.W., Carranza, E., Sjogren, W.L., Yuan, D.N., 2001. Recent gravity models as a result of the Lunar Prospector mission. Icarus 150, 1–18.

Konopliv, A.S., Binder, A.B., Hood, L.L., Kucinskas, A.B., Sjogren, W.L., Williams, J.G., 1998. Improved gravity field of the Moon from Lunar Prospector. Science 281, 1476–1480.

Leinenweber, K.D., Tyburczy, J.A., Sharp, T.G., Soignard, E., Diedrich, T., Petuskey, W.B., Wang, Y., Mosenfelder, J.L., 2012. Cell assemblies for reproducible multi-anvil experiments (the COMPRESS assemblies). Am. Mineral. 97, 353–368.

Li, J., Fei, Y., 2003. Experimental constraints on core composition. In: Carlson, R.W., Turekian, K.K. (Eds.), The Mantle and Core. Elsevier, pp. 1–31.

Lognonné, P., Johnson, C.L., 2007. Planetary seismology. In: Spohn, T. (Ed.), Planets and Moons. Elsevier, p. 69.

Lyttleton, R.A., 1965. On the internal structure of the planet Mars. Mon. Not. R. Astron. Soc. 129, 21–39.

Morard, G., Sanloup, C., Fiquet, G., Mezouar, M., Rey, N., Poloni, R., Beck, P., 2007. Structure of eutectic Fe–FeS melts to pressures up to 17 GPa: implications for planetary cores. Earth Planet. Sci. Lett. 263, 128–139.

Murnaghan, F.D., 1967. Finite Deformation of an Elastic Solid. Dover, New York.

Nasch, P.M., Manghnani, M.H., Secco, R.A., 1997. Anomalous behavior of sound velocity and attenuation in liquid Fe–Ni–S. Science 277, 219–221.

Nishida, K., Kono, Y., Terasaki, H., Takahashi, S., Ishii, M., Shimoyama, Y., Higo, Y., Funakoshi, K.-I., Irifune, T., Ohtani, E., 2013. Sound velocity measurements in liquid Fe–S at high pressure: implications for Earth's and lunar cores. Earth Planet. Sci. Lett. 262, 182–186.

Sanloup, C., Fiquet, G., Gregoryanz, E., Morard, G., Mezouar, M., 2004. Effect of Si on liquid Fe compressibility: implications for sound velocity in core materials. Geophys. Res. Lett. 31, L07604. http://dx.doi.org/10.1029/2004GL019526.

Sanloup, C., Guyot, F., Gillet, P., Fei, Y., 2002. Physical properties of liquid Fe alloys at high pressure and their bearings on the nature of metallic planetary cores. J. Geophys. Res. 107, 2272. http://dx.doi.org/10.1029/2001JB000808.

Sanloup, C., Guyot, F., Gillet, P., Fiquet, G., Mezouar, M., Martinez, I., 2000. Density measurements of liquid Fe–S alloys at high-pressure. Geophys. Res. Lett. 27, 811–814.

Shea, E.K., Weiss, B.P., Cassata, W.S., Shuster, D.L., Tikoo, S.M., Gattacceca, J., Grove, T.L., Fuller, M.D., 2012. A long-lived lunar core dynamo. Science 335, 453–456.

Shimizu, H., Matsushima, M., Takahashi, F., Shibuya, H., Tsunakawa, H., 2013. Constraint on the lunar core size from electromagnetic sounding based on magnetic field observations by an orbiting satellite. Icarus 222, 32–43.

Smith, D.E., Zuber, M.T., Neumann, G.A., Lemoine, F.G., 1997. Topography of the Moon from the Clementine Lidar. J. Geophys. Res. 102, 1591–1611.

Stacey, F.D., 2005. High pressure equations of state and planetary interiors. Rep. Prog. Phys. 68, 341–383.

Stegman, D.R., Jellinek, A.M., Zatman, S.A., Baumgardner, J.R., Richards, M.A., 2003. An early lunar core dynamo driven by thermochemical mantle convection. Nature 421, 143–146.

Stixrude, L., Lithgow-Bertelloni, C., 2005. Thermodynamics of mantle minerals – I. Physical properties. Geophys. J. Int. 162, 610–632.

Strong, H.M., Tuft, R.E., Hanneman, R.E., 1973. The iron fusion curve and γ-δ-l triple point. Metall. Trans. 4, 2657–2661.

Tange, Y., Nishihara, Y., Tsuchiya, T., 2009. Unified analyses for P-V-T equation of state of MgO: a solution for pressure-scale problems in high P-T experiments. J. Geophys. Res. 114, B03208. http://dx.doi.org/10.1029/2008JB005813.

Terasaki, H., Suzuki, A., Ohtani, E., Nishida, K., Sakamaki, T., Funakoshi, K., 2006. Effect of pressure on the viscosity of Fe–S and Fe–C liquids up to 16 GPa. Geophys. Res. Lett. 33, L22307. http://dx.doi.org/10.1029/2006GL027147.

van Kan Parker, M., Sanloup, C., Sator, N., Guillot, B., Tronche, E.J., Perrillat, J.-P., Mezouar, M., Rai, N., van Westrenen, W., 2012. Neutral buoyancy of titanium-rich melts in the deep lunar interior. Nat. Geosci. 5, 186–189.

Wang, Y., Rivers, M.L., Sutton, S.R., Nishiyama, N., Uchida, T., Sanehira, T., 2009. The large-volume high-pressure facility at GSECARS: a "Swiss-army-knife" approach to synchrotron-based experimental studies. Phys. Earth Planet. Inter. 174, 270–281.

Weber, R.C., Lin, P.-Y., Garnero, E.J., Williams, Q., Lognonné, P., 2011. Seismic detection of the lunar core. Science 331, 309–312.

Wieczorek, M.A., Jolliff, B.L., Khan, A., Pritchard, M.E., Weiss, B.P., Williams, J.G., Hood, L.L., Righter, K., Neal, C.R., Shearer, C.K., McCallum, I.S., Tompkins, S., Hawke, B.R., Peterson, C., Gillis, J.J., Bussey, B., 2006. The constitution and structure of the lunar interior. In: Jolliff, B.L., Wieczorek, M.A., Shearer, C.K., Neal, C.R. (Eds.), New Views of the Moon. Mineralogical Society of America, pp. 221–364.

Wieczorek, M.A., Neumann, G.A., Nimmo, F., Kiefer, W.S., Taylor, G.J., Melosh, H.J., Phillips, R.J., Solomon, S.C., Andrews-Hanna, J.C., Asmar, S.W., Konopliv, A.S., Lemoine, F.G., Smith, D.E., Watkins, M.M., Williams, J.G., Zuber, M.T., 2013. The crust of the Moon as seen by GRAIL. Science 339, 671–675.

Williams, J.G., Boggs, D.H., Yoder, C.F., Ratcliff, J.T., Dickey, J.O., 2001. Lunar rotational dissipation in solid body and molten core. J. Geophys. Res. 106, 27933–27968.

Williams, Q., 2009. Bottom-up versus top–down solidification of the cores of small solar system bodies: constraints on paradoxical cores. Earth Planet. Sci. Lett. 284, 564–569.